

CARL: Camera-Agnostic Representation Learning for Spectral Image Analysis

Alexander Baumann^{1,2,3,*} Leonardo Ayala² Silvia Seidlitz^{2,4,5,6}
 Jan Sellner^{2,5,6} Alexander Studier-Fischer^{7,8,9,10} Berkin Özdemir^{8,9,10}
 Lena Maier-Hein^{2,3,4,5,6,†}, Slobodan Ilic^{1,†}

¹ Siemens AG, Munich

² Division of Intelligent Medical Systems, German Cancer Research Center (DKFZ) Heidelberg

³ Medical Faculty and ⁴ Faculty of Mathematics and Computer Science, Heidelberg University

⁵ National Center for Tumor Diseases (NCT), NCT Heidelberg

⁶ HIDSS4Health, Heidelberg

⁷ Department of Urology and Urosurgery, University Medical Center Mannheim

⁸ Department of General, Visceral, and Transplantation Surgery, Heidelberg University Hospital

⁹ Division of Intelligent Systems and Robotics in Urology, DKFZ Heidelberg

¹⁰ DKFZ Hector Cancer Institute, University Medical Center Mannheim

Abstract

*Spectral imaging offers promising applications across diverse domains, including medicine and urban scene understanding, and is already established as a critical modality in remote sensing. However, variability in channel dimensionality and captured wavelengths among spectral cameras impede the development of AI-driven methodologies, leading to camera-specific models with limited generalizability and inadequate cross-camera applicability. To address this bottleneck, we introduce **CARL**, a model for **Camera-Agnostic Representation Learning** across RGB, multispectral, and hyperspectral imaging modalities. To enable the conversion of a spectral image with any channel dimensionality to a camera-agnostic embedding, we introduce wavelength positional encoding and a self-attention-cross-attention mechanism to compress spectral information into learned query representations. Spectral-spatial pre-training is achieved with a novel spectral self-supervised JEPA-inspired strategy tailored to CARL. Large-scale experiments across the domains of medical imaging, autonomous driving, and satellite imaging demonstrate our model’s unique robustness to spectral heterogeneity, outperforming on datasets with simulated and real-world cross-camera spectral variations. The scalability and versatility of the proposed approach position our model as a backbone for future spectral foundation models.*

1. Introduction

Spectral Imaging, including RGB, multispectral, and hyperspectral imaging, capture channel-wise reflectance information for camera-specific wavelengths. The enriched spectral information, contained in a few to hundreds of channels, enables applications in a variety of fields, including segmentation and classification tasks in medicine [2, 33], urban scene perception [34, 36], and remote sensing [29, 37]. To develop robust solutions for these tasks, data-driven models have emerged as the prevailing standard, maximizing performance through the utilization of all available images, regardless of camera characteristics. However, the evolution of spectral imaging technology has resulted in significant variability in camera devices [31], leading to the formation of camera-specific data silos. These silos share valuable domain-specific geometric information but differ in spectral characteristics such as channel dimensionality and covered wavelengths. Conventional imaging models such as Convolutional Neural Networks (CNNs) [20] cannot accommodate for these variations, resulting in camera-specific models and absent knowledge transfer between these data silos. Therefore, such models ignore large amounts of data, limiting their robustness and cross-applicability. Furthermore, supervised downstream models are inherently limited by the availability of application-specific annotations. Given that manual labeling is time-intensive and often infeasible for large-scale datasets, self-supervised pre-training has emerged as a powerful alternative [7, 13, 21, 22]. Empirical findings in Natural Language Processing have demonstrated that the effectiveness of self-supervised-learning

*Corresponding Author: baumann.alexander@siemens.com

†Equal Contribution

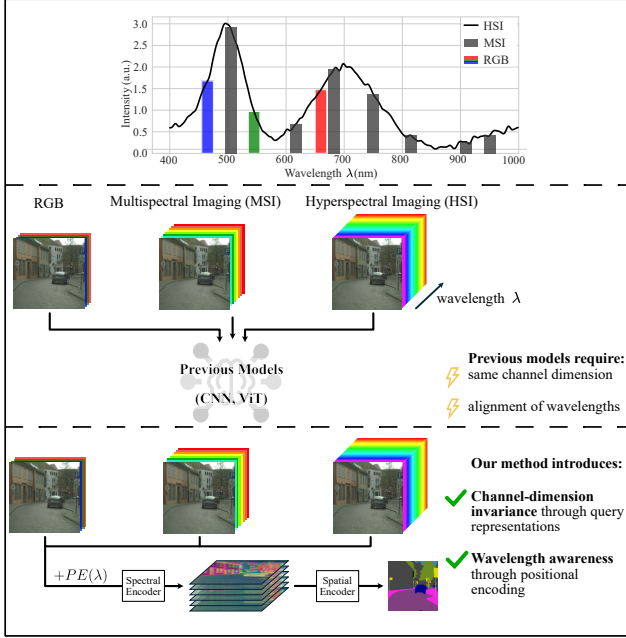


Figure 1. **The proposed model addresses spectral camera variations by extracting camera-agnostic representations.** In contrast to existing models, which require independent training data for spectral cameras with varying channel dimensions and filter responses, the proposed approach enables cross-camera generalization through the incorporation of wavelength positional encoding $PE(\lambda)$. Additionally, it achieves invariance to channel dimensionality by extracting inter-channel relationships and compressing them in a fixed set of learned query representation.

(SSL) scales with the amount of training samples [25]. This motivates the use of extensive cross-silo datasets to enhance pre-training. However, existing strategies are not camera-agnostic, restricting pre-training to camera-specific data silos and limiting their effectiveness. To overcome these obstacles, we propose a novel camera-agnostic model with a tailored self-supervised pre-training strategy that is capable of unlocking the data treasures of different cameras that are not yet accessible (Fig. 1). Our contribution is threefold:

1. **First approach to spectral-spatial camera-agnostic representation learning:** We propose the first method that enables spectral-spatial encoding in a wavelength-aware manner. To this end, we introduce wavelength positional encoding for establishing cross-camera channel correspondences, and learnable query representations for efficient representation learning.
2. **First camera-agnostic spectral-spatial self-supervised framework:** Inspired by recent successes in temporal and spatial self-supervision, we propose a novel spectral self-supervised pre-training strategy tailored to our model that is seamlessly integrated with the I-JEPA spatial self-supervised strategy [1] to

form an end-to-end framework for camera-agnostic spectral-spatial self-supervised pre-training.

3. **Large-scale cross-domain validation:** We validated the proposed model on experiments across three domains, namely organ segmentation, urban scene segmentation, and land cover classification. Across all experiments, the model exhibits unique robustness to spectral heterogeneity based on simulated and real-world camera variations, compared to existing camera-specific and channel-invariant baselines.

2. Related Work

Encoding Strategies for Spectral Imaging. Generating rich image representations remains a fundamental problem in computer vision, critically influencing downstream applications such as image segmentation. In the context of 2D spectral images, the encoding process inherently encompasses three dimensions: the two spatial dimensions and the channel dimension. However, in datasets with uniform spectral properties, conventional imaging models, such as CNNs or Vision Transformers (ViTs), are frequently employed, which exclusively perform spatial encoding [5, 14, 33, 36]. Recently, SatMAE [10], SpectralGPT+ [24] and SpectralEarth [6] were proposed as spectral imaging models in remote sensing that incorporate both spectral and spatial encoding. The former two models employ joint spatial and spectral encoding, utilizing self-attention across spatial-spectral patches. However, both are not invariant to the channel dimension, rendering them inapplicable for cross-camera datasets. Conversely, SpectralEarth is capable of processing spectral images with an arbitrary number of channels. It introduces the so-called Spectral Adapter that encodes and ultimately resolves the channel dimension through 1D convolutions and pooling operations. Subsequently, the model captures spatial relations via a standard spatial encoder, such as ViT [14]. However, the Spectral Adapter disregards cross-camera channel relations based on camera-specific wavelength information. In contrast, the wavelength-aware Hyve layer was proposed as a novel first layer of a CNN to address these limitations [38]. This layer projects spectral images to feature space in a wavelength-aware manner prior to spatial encoding. Specifically, each channel is convolved with a learned linear combination of a fixed number of kernels, where the linear coefficients are determined by the channel’s respective wavelength. However, Hyve-based CNNs do not explicitly extract inter-channel correspondences due to their restriction to 2D convolutions. Consequently, the model’s capacity to generate rich spectral features on cross-camera datasets with spectral heterogeneity is likely limited. Conversely, models that exclusively encode along the channel dimension for each pixel or patch were also proposed for spectral imaging tasks [19, 23]. However, such approaches cannot learn geometric

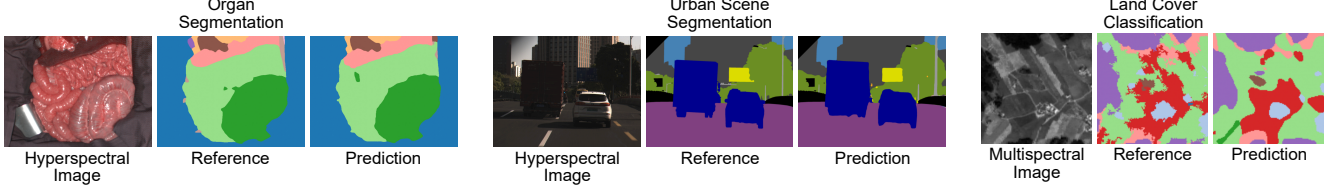


Figure 2. **CARL, the proposed model, serves as a universal backbone for spectral imaging tasks.** Across three experiments, encompassing diverse applications of spectral imaging, our model demonstrated superior performance over baselines.

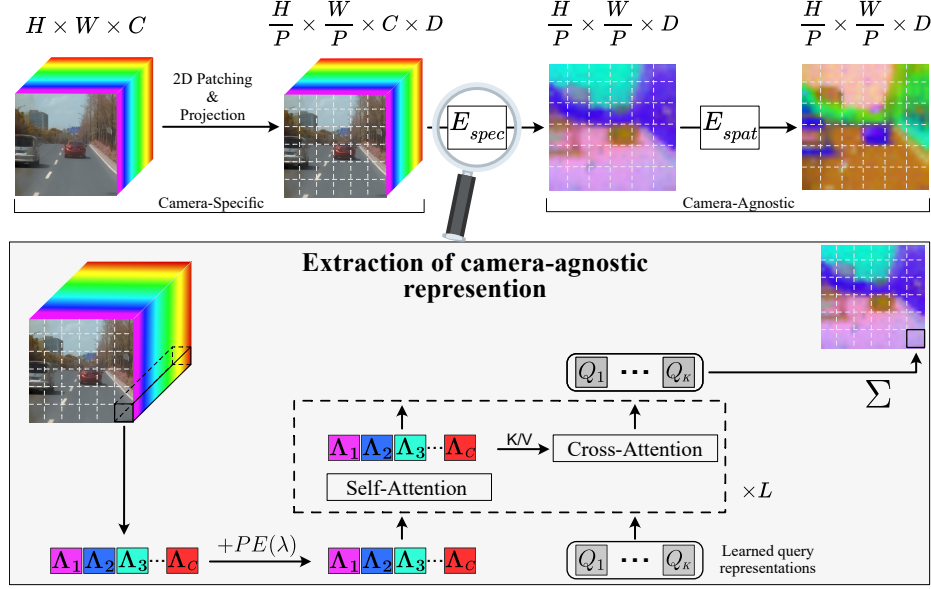


Figure 3. **Core concept: Conversion of a camera-specific spectral image into a camera-agnostic representation.** To address the heterogeneity in camera-dependent spectral properties, a dedicated spectral encoder extracts a camera-agnostic representation by leveraging spectral tokens that encode the wavelength information. To this end, a spectral image of dimension $H \times W \times C$ is first divided into patches of size $P \times P$, which are band-wise projected to D -dimensional feature space. The spectral encoder E_{spec} processes each patch individually, and hereby resolves the spectral dimension. In particular, E_{spec} encodes the wavelength λ_i of channel i as positional encoding $PE(\lambda_i)$ and adds it to the corresponding embedded patch Λ_i . Self-Attention among the spectral tokens $(\Lambda_i)_{i \leq C}$ and alternating Cross-Attention towards K learned queries $(Q_j)_{j \leq K}$ yield enriched query representations. These representations are then aggregated through summation to form the camera-agnostic representation. Finally, spatial relations are captured by a common transformer-based image encoder E_{spat} .

structures by design, significantly limiting performance in downstream applications. This observation underscores the necessity for camera-agnostic model architectures, capable of generating rich representations that are both spectrally and spatially aware.

Self-Supervised Strategies for Spectral Imaging. With an increase of compute resources and available data, self-supervised pre-training strategies have gained importance in recent years [18]. Consequently, SSL techniques have been explored for conventional imaging models such as ViT [14]. Masked image modeling [22] presents a prominent paradigm, wherein input patches are randomly masked and subsequently reconstructed via a process of comprehensive encoding and light-weight decoding. As reconstruction in pixel space is sensitive and requires large amounts

of data and compute resources, more efficient pre-training concepts have been explored, which operate exclusively in feature space [1, 7, 21]. In particular, a masking strategy within the feature space, namely I-JEPA [1], has been proposed, demonstrating enhanced downstream performance with reduced training duration. Notably, the mentioned self-supervised strategies exclusively learn spatial relations, ignoring valuable inter-channel correspondences of spectral images. In contrast, models tailored to remote sensing tasks such as SpectralGPT⁺ proposed masked image modeling for spatial-spectral patches instead [10, 24, 32]. However, these models are not applicable on cross-camera datasets, restricting them to camera-specific pre-training dataset.

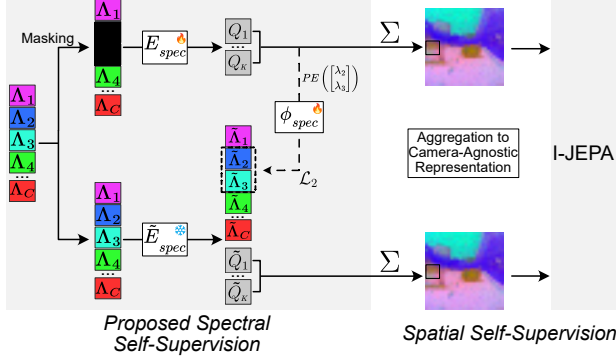


Figure 4. **Our new approach to spectral self-supervision enables the joint learning of camera-agnostic representations and spatial relations.** Spectral self-supervision involves patch-wise reconstruction of masked spectral channels in the feature space. The student encoder E_{spec} extracts query representations $(Q_j)_{j \leq K}$ from a spectrally masked input patch, while the predictor ϕ_{spec} predicts the masked spectral tokens using encoded wavelengths (here: λ_2, λ_3), and the representations $(Q_j)_{j \leq K}$. Target tokens are generated by the teacher encoder \tilde{E}_{spec} from the complete input. The aggregated camera-agnostic representations are subsequently processed by the I-JEPA spatial SSL strategy [1], integrated within an end-to-end pre-training framework.

3. Framework for camera-agnostic spectral image analysis

In this paper, we present CARL, a novel model for spectral image processing, designed to unlock the potential of camera-specific spectral data silos. As illustrated in Fig. 3, the proposed framework transforms camera-dependent spectral information into a camera-agnostic representation through a novel spectral encoder E_{spec} , followed by the extraction of geometric information through a standard transformer-based spatial encoder E_{spat} . To establish cross-camera channel correspondences, we translate the concept of positional encoding, traditionally used for discrete token positions within transformers [39], to channel-specific wavelengths. For efficient representation learning along the channel dimension, we learn salient spectral information within a sparse set of query representations, inspired by [27]. Ultimately, the spectral encoder extracts a 2D camera-agnostic representation enriched with spectral attributes that can be seamlessly forwarded to established transformer-based spatial encoders, exemplified by ViT [14]. The spatial encoder E_{spat} operates subsequent to E_{spec} and enhances feature representation by capturing spatial relationships. Two learning paradigms are proposed to optimize the derived query representations. Specifically, these representations are either learned implicitly by minimizing a task-specific loss, such as a segmentation loss, or explicitly by minimizing a self-supervised loss (CARL-SSL, as described in Sec. 3.2).

3.1. Architecture of CARL

Given a spectral image $I \in \mathbb{R}^{H \times W \times C}$ with arbitrary channel dimension, C , the objective is to derive a camera-agnostic representation that contains salient spectral information. To project I to feature space, each channel is processed by a shared 2D convolution with kernel size and stride equal to the patch size P and output channels D , yielding a tensor of dimensionality $\frac{H}{P} \times \frac{W}{P} \times C \times D$. A patch, denoted as $\Lambda = (\Lambda_1, \dots, \Lambda_C) \in \mathbb{R}^{C \times D}$, is then independently processed by the spectral encoder, E_{spec} , to generate a camera-agnostic representation. To this end, we first construct a positional encoding $PE(\lambda) \in \mathbb{R}^{C \times D}$ where $\lambda = (\lambda_1, \dots, \lambda_C)$ and λ_i corresponds to the wavelength of channel i such that the model is capable of establishing channel correspondences across cameras with different wavelength specifications. In this work, we employ the sinusoidal Fourier Features [35] to encode positional information within the spectral dimension, defined as:

$$PE(\lambda_i) = [\cos(2\pi\alpha\lambda_i B), \sin(2\pi\alpha\lambda_i B)]^T \in \mathbb{R}^D \quad (1)$$

where $\alpha \in \mathbb{R}$ is a scaling factor, $B \sim \mathcal{N}(0, \sigma^2 \mathbf{I}) \in \mathbb{R}^{D/2}$, and $\sigma \in \mathbb{R}$. Here, both α and σ are hyperparameters. Subsequently, $PE(\lambda)$ is added to the patch Λ , thereby encoding the position of each Λ_i along the wavelength axis. As illustrated in Fig. 3, a self-attention-cross-attention module is subsequently employed to process the spectral tokens, $(\Lambda_i)_{i \leq C}$, and derive query representations. Specifically, K learnable D -dimensional query representations, denoted as $(Q_j)_{j \leq K}$, are initialized from a truncated normal distribution. Following a self-attention block applied to the spectral tokens, these query representations, $(Q_j)_{j \leq K}$, attend to the spectral tokens, $(\Lambda_i)_{i \leq C}$, via cross-attention, effectively compressing the most salient information. This self-attention-cross-attention module is iterated L times to learn enriched query representations, $(Q_j)_{j \leq K}$. Subsequently, a readout function, in this instance summation, is applied to $(Q_j)_{j \leq K}$ to aggregate the information into a camera-agnostic representation for the patch Λ . As the spectral encoder generates such a representation for each patch independently, the incorporation of spatial relationships necessitates the utilization of a subsequent spatial encoder. It is noteworthy that since E_{spec} has encoded device-dependent spectral properties within the feature space, most common transformer-based spatial encoders, such as ViT [14] or Swin Transformer [28], may be employed for spatial encoding. To ensure dimensional compatibility between the spectral and spatial encoder, layer normalization and a linear transformation are applied prior to spatial encoding. After capturing inter-patch relationships, a task-specific head can be added for the intended downstream application.

3.2. Self-Supervised Training Strategy

Tailored to the CARL framework (Sec. 3.1), we propose a self-supervised pre-training strategy, CARL-SSL, to leverage large-scale unlabeled datasets. As illustrated in Fig. 4, the procedure is partitioned into spectral and spatial self-supervised pre-training within an end-to-end framework. For each stage, we employ the Joint-Embedding-Predictive-Architecture (JEPA) paradigm [26]. While I-JEPA [1] is adapted for spatial self-supervision, we introduce a novel JEPA-based spectral SSL strategy.

Specifically, given student encoders, E_{spec} and E_{spat} from Sec. 3.1, and corresponding teacher encoders, \tilde{E}_{spec} and \tilde{E}_{spat} , with exponential moving average weights, we mask specific regions of the students’ input, with the objective to predict the corresponding features generated by the teachers via predictors ϕ_{spec} and ϕ_{spat} . It is noteworthy that the loss function is decomposed into a spectral and a spatial component.

For an image $I \in \mathbb{R}^{H \times W \times C}$, the initial convolution is applied as described in Sec. 3.1. A spectral mask, denoted by $M \subseteq \{1, \dots, C\}$, containing the masked channel indices, is sampled for a patch Λ , and the unmasked tokens, denoted by $(\Lambda_i)_{i \notin M}$, are forwarded to the student spectral encoder, E_{spec} , to generate query representations, $(Q_j)_{j \leq K}$ (see Fig. 4). Conversely, the teacher spectral encoder receives all spectral tokens as input, producing learned spectral tokens, $(\tilde{\Lambda}_i)_{i \leq C}$, via self-attention, and query representations, $(\tilde{Q}_j)_{j \leq K}$. The objective of spectral pre-training is then to predict the masked spectral tokens, $(\tilde{\Lambda}_i)_{i \in M}$, based on the extracted student query features, $(Q_j)_{j \leq K}$, and the positional encoding of the masked wavelengths. To this end, a transformer-based predictor, denoted by ϕ_{spec} , is employed, receiving as input a sequence with the query representations and dedicated mask tokens [13]. The mask tokens are $|M|$ copies of a shared, learnable embedding and are summed with wavelength positional encoding $(PE(\lambda_i))_{i \in M}$, corresponding to the masked wavelengths. Subsequently, ϕ_{spec} processes this sequence through multiple self-attention blocks, resulting in learned mask tokens as predictions for $(\tilde{\Lambda}_i)_{i \in M}$. Network optimization is performed using the VICReg loss [3], which comprises invariance, variance, and covariance terms. The invariance term quantifies the mean-squared error between predicted and target spectral tokens, while the variance and covariance terms contribute to training stability and the prevention of feature collapse.

For simultaneous training of the spatial encoder, the query representations from both the student and teacher encoders are summed and aggregated across the patches to generate 2D camera-agnostic representations. Subsequently, a 2D region of the student’s feature representation is masked, and the remaining spatial tokens are pro-

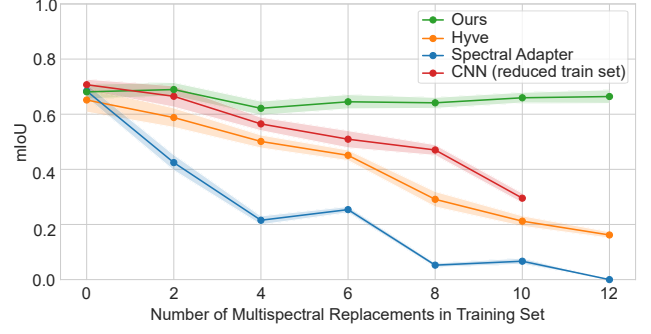


Figure 5. **Our model demonstrates unique robustness to heterogeneity in spectral properties.** As spectral heterogeneity increases with the number of multispectral replacements in the training set, our model uniquely maintains a high mIoU score on the hyperspectral test set. Notably, it sustains strong performance even when the training set does not include any hyperspectral images (i.e., when the number of multispectral replacements reaches 12). The shaded area represents the 95 % confidence interval.

cessed by E_{spat} . In a manner analogous to the spectral pre-training, the spatial predictor, denoted as ϕ_{spat} , receives the extracted non-masked features and positional encoding of the masked tokens as input, predicting corresponding features extracted by the teacher spatial encoder, \tilde{E}_{spat} [1]. The spatial loss function is also defined using the VICReg loss. Finally, the spatial and spectral loss components are equally-weighted summed to jointly optimize student encoders and predictors. It is noteworthy that this pre-training strategy can be accelerated by employing multiple spectral and spatial masks.

3.3. Implementation Details

Following ablation studies (see Sec. 5), we set $\sigma = 3$, as defined in Eq. (1) for the wavelength positional encoding, and the number of query representations within the spectral encoder to $K = 8$. Further implementation details of the model are outlined in the supplementary. Unless otherwise stated in the experiments, we employed EVA-02 [15] as spatial encoder, which is a modern version of ViT [14]. To perform semantic segmentation, the model was integrated with the ViT-Adapter for hierarchical feature generation [8], and the UperNet segmentation head [41].

4. Experiments and results

This experimental study aimed to address the following research questions pertaining to the proposed model:

- (RQ1) In silico proof of concept: Does the spectral representation learning approach enable effective knowledge transfer across cameras?
- (RQ2) Real-world cross-domain generalization: To what extent do CARL and CARL-SSL help in handling real-world cross-camera variations?

	Camera-specific	Spectral Adapter [6]	Hyve [38]	CARL	CARL-SSL
mIoU	44.6 [40.9; 47.3]	43.4 [41.0; 45.2]	48.0 [45.4; 50.0]	48.6 [45.6; 51.0]	50.1 [47.2; 52.4]

Table 1. **The proposed spectral encoder demonstrates superior performance as a camera-agnostic model.** The mIoU scores with the 95 % confidence intervals on the HSICity test set. While the camera-specific model was pre-trained on Cityscapes and fine-tuned exclusively on HSICity, the other models are channel-invariant adaptations which were concurrently trained on both datasets. Notably, our spectral encoder performs best among the presented adaptation methods, and significantly benefits from self-supervised pre-training.

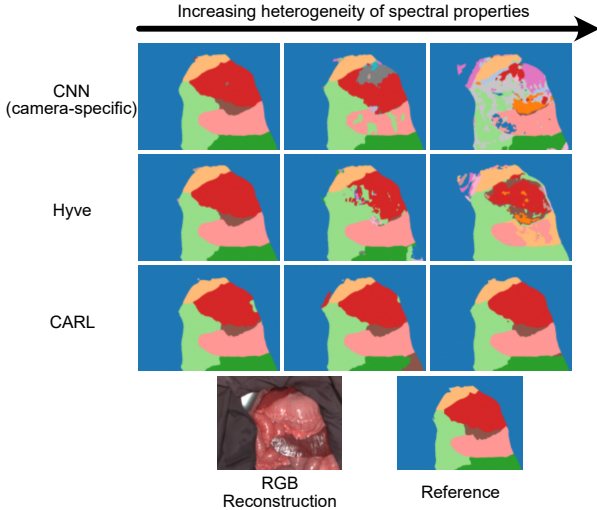


Figure 6. **Our model maintains accurate predictions despite progressive increases in spectral heterogeneity.** As the spectral heterogeneity within the training set progressively increases from left to right, a significant increase in prediction noise is observed for both the camera-specific CNN and the Hyve model. In contrast, our model, CARL, consistently provides accurate predictions across all camera configurations.

While (RQ1) is addressed in the first experiment, (RQ2) was investigated in the second and third experiments. All experiments involved semantic segmentation tasks, with model performance quantified using class-wise Intersection-over-Union (IoU).

4.1. In silico proof of concept: Medical imaging

Datasets. Synthetic multispectral images were generated from a real hyperspectral dataset, allowing for isolated control of spectral variations while preserving spatial context. A private dataset of pig organ images, semantically annotated with 19 classes, served as the hyperspectral dataset [33]. The images were acquired by a Tivita® Tissue HSI camera (Diaspective Vision GmbH, Am Salzhaff,

Germany) and exhibit 100 spectral channels ranging from 500 nm to 1,000 nm. The training set consists of 254 images from 12 subjects.

In general, multispectral imaging employ optical filters that measure reflectance values within specific wavelength ranges. To synthesize realistic multispectral images, we replicated this acquisition process by simulating corresponding filter functions. A detailed description is outlined in the supplementary. Each filter function, representing a distinct multispectral channel, was modeled as a L1-normalized Gaussian distribution, with the mean parameter corresponding to the filter’s center wavelength. The number of channels, C , for each simulated camera was uniformly sampled between 10 and 25, and C channel-specific center wavelengths, ranging from 550 nm to 950 nm, were selected using farthest point sampling. Given filter functions of one real near-infrared multispectral camera with 25 channels, Gaussian distributions were fitted to determine a representative variance interval, from which C variance values were subsequently sampled. For the resulting filter functions $F \in \mathbb{R}^{C \times 100}$, evaluated at the channel wavelengths of the provided hyperspectral dataset, a corresponding multispectral image $\tilde{I} \in \mathbb{R}^{H \times W \times C}$ was then simulated from a hyperspectral image $I \in \mathbb{R}^{H \times W \times 100}$ via matrix multiplication.

In this experiment, six camera configurations were simulated, resulting in six sets of synthetic multispectral images. To systematically introduce spectral heterogeneity into the original hyperspectral training data, a progressive substitution strategy with the synthetic multispectral images was employed. In each iteration, hyperspectral data from two additional porcine subjects was substituted with the corresponding synthetic multispectral images from a different simulated camera configuration. This process yielded six augmented datasets exhibiting increasing spectral heterogeneity while maintaining the surgical scene content. Model generalization to hyperspectral imagery was evaluated on the original hyperspectral test set, encompassing 166 images from five different pig subjects.

Baseline Methods. The model performance was benchmarked against a camera-specific baseline model and two channel-invariant adaptation methods: the Hyve layer [38] and the Spectral Adapter [6]. The camera-specific model is a traditional U-Net, which represents the state of the art on the original hyperspectral dataset [33], and was trained exclusively on the hyperspectral subset of each training set variant. The Hyve layer was coupled with the camera-specific U-Net, while the Spectral Adapter was integrated in the same way as our spectral encoder.

Results. The mean Intersection over Union (mIoU) scores as a function of the number of multispectral replacements within the training set is presented in Fig. 5. The proposed method uniquely maintained a high mIoU across all train-

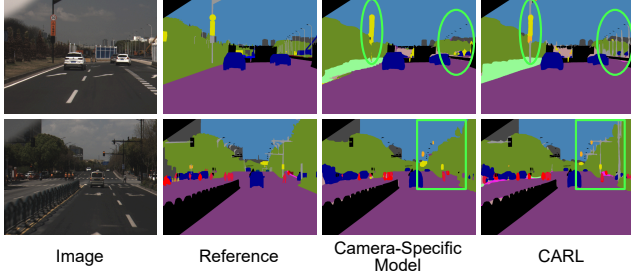


Figure 7. **The proposed model enables cross-modality knowledge transfer.** Two examples from the HSICity test set show that our model successfully leveraged RGB data to compensate for missing classes. The camera-specific model, pre-trained on the RGB dataset Cityscapes and subsequently fine-tuned on hyperspectral dataset HSICity, demonstrates an inability to segment "poles" due to the absence of this class within the HSICity training set. In contrast, CARL, trained concurrently on Cityscapes and HSICity, effectively leverages the "pole" annotations from Cityscapes to inform its predictions on HSICity.

ing set variants. This is qualitatively confirmed in Fig. 6, where prediction noise of the baseline methods increases with spectral heterogeneity, while our model remains stable and accurate. Notably, both channel-invariant baselines performed inferiorly to the camera-specific model, despite the latter being exposed to fewer surgical scenes during training. In the most extreme scenario, where the dataset consisted exclusively of multispectral images, CARL improved upon Hyve by 50.2 mIoU.

4.2. Real-world evaluation: Automotive

The purpose of the second experiment was to test the capabilities of our approach under real-world conditions in the context of autonomous driving. Specifically, we investigated whether our model can effectively leverage RGB, and hyperspectral images for a hyperspectral downstream task, namely urban scene segmentation.

Datasets. The Cityscapes RGB dataset [11], which comprises semantic annotations for 19 classes, was utilized in conjunction with its hyperspectral counterpart, HSICity [34]. HSICity consists of hyperspectral images with 128 channels (450 nm to 950 nm) and shares the same semantic classes. However, substantial challenges arise from its training set due to coarse annotations and class imbalances. For instance, the "pole" class, while present in the test set, is absent from the training set annotations. To mitigate these limitations, finely annotated images from the Cityscapes training set, which include the "pole" class, were incorporated. The final training set consisted of 4,029 images, including 1,054 images from HSICity, while the HSICity test set with fine-grained annotations encompasses 276 images. To evaluate cross-camera generalization, training was conducted on the aggregated training set and subsequent valida-

tion on the HSICity test set. For the pre-training phase, we leveraged a diverse collection of spectral urban datasets, including Cityscapes, HSICity, and the multispectral datasets HyKo-VIS [40] and HSIDrive [4].

Experimental Setup & Baseline Methods. In this experiment, a Swin Transformer [28] with a Mask2Former head [9], referred to as SwinMask2Former, pre-trained on the Cityscapes dataset, was adapted through the integration of a channel-invariant module. Our spectral encoder, serving as this module, was compared to the Hyve layer, and the Spectral Adapter. Additionally, as a camera-specific baseline, the pre-trained SwinMask2Former, devoid of a channel-invariant adaptation, was trained exclusively on HSICity. To assess the benefit of the proposed pre-training strategy, our spectral encoder within SwinMask2Former was initialized using weights obtained through the tailored SSL strategy.

Results. The mIoU scores on the HSICity test set are presented in Tab. 1. The proposed spectral encoder (pre-trained and non-pre-trained) demonstrated superior performance compared to the baseline methods. Due to the absence of the "pole" class in the HSICity training set, the conventional camera-specific model, exclusively trained on HSICity, failed to segment any poles in the test set, despite its pre-training (see Fig. 7). In contrast, our model effectively transferred knowledge from the "pole" annotations in Cityscapes to improve its predictions on HSICity. Notably, the proposed model exhibited the highest IoU score for the "pole" class, as can be seen in the supplementary. At last, CARL-SSL demonstrated its effectiveness by outperforming our non-pre-trained model by about 1.5 mIoU.

4.3. Real-world evaluation: Satellite imaging

The purpose of the third experiment was to test the real-world capabilities of our self-supervision approach in a third application domain, namely satellite imaging. Specifically, we examined whether the proposed self-supervised pre-training on hyperspectral satellite images enhances the downstream performance on multispectral images in the context of land cover classification.

Dataset. The SegMunich land cover dataset [24], consisting of images with ten spectral bands from 442 nm to 2,185 nm and semantic annotations for twelve land cover classes, served as the downstream dataset. For the pre-training phase, the HySpecNet-11k hyperspectral remote sensing dataset [16] was employed, encompassing 11,483 image patches and offering a substantially higher spectral resolution with 202 bands spanning from 418 nm to 2,445 nm.

Baseline Methods. The efficacy of the proposed model was benchmarked against methods presented in [24]. Among these, SpectralGPT⁺ [24], a camera-specific spectral foundation model and the state of the art method on the SegMu-

Method	Pre-training data	Arable land	Perm. Crops	Pastures	Forests	Surface water	Shrub	Open spaces	Wetlands	Mine, dump	Artificial veg.	Urban fabric	Buildings	mIoU
SatMAE [10]	> 700,000 MSI	72.3	15.8	49.7	81.9	74.0	13.6	27.5	41.2	37.9	18.3	65.3	50.6	45.7
SpectralGPT ⁺ [24]	> 1,000,000 MSI	73.1	22.5	51.0	84.1	76.0	14.5	33.7	39.6	38.7	22.5	67.4	52.0	47.9
retrained SpectralGPT ⁺	> 1,000,000 MSI	72.2	21.9	51.0	86.3	76.5	17.2	44.0	39.0	48.2	22.9	66.8	53.3	49.1 [48.6; 49.6]
CARL-SSL	> 11,000 HSI	72.7	24.6	51.4	86.5	76.5	21.2	45.0	40.5	41.3	26.2	68.2	54.4	50.7 [50.2; 51.2]

Table 2. **Efficient hyperspectral pre-training yields superior multispectral downstream performance.** Class-wise IoU scores on the SegMunich multispectral land cover dataset were benchmarked against two camera-specific self-supervised pre-trained models. Despite the baseline methods utilizing a significantly larger multispectral pre-training dataset, the proposed model demonstrates superior performance through efficient hyperspectral pre-training. The 95 % confidence intervals are written in gray if available.

nich dataset, was re-trained from its self-supervised checkpoint using the identical training protocol as our model, ensuring a fair evaluation.

Results. Quantitative results for the twelve land cover classes of the SegMunich dataset, are presented in Tab. 2. Notably, our model demonstrates a +1.6 mIoU improvement compared to the state of the art SpectralGPT⁺. This performance gain is achieved despite utilizing a pre-training dataset that is only 1 % of the size of the SpectralGPT⁺ dataset, albeit with higher spectral resolution. Furthermore, our initialization strategy yields substantial benefits for challenging classes characterized by low IoU scores, such as "Artificial Vegetation", "Shrub", and "Permanent Crops". As outlined in the supplementary, SpectralGPT⁺ also exhibits higher computational costs compared to CARL.

5. Ablation Study

The previous experiments have clearly demonstrated the ability of CARL to derive rich camera-agnostic representations in the presence of spectral heterogeneity, resulting in enhanced downstream performance. The purpose of this ablation study was to assess the efficacy of CARL’s key architectural components, specifically the wavelength positional encoding and the query representations, and to determine their optimal hyperparameter configurations. The ablation studies were conducted on a training dataset variant from Sec. 4.1, characterized by diverse spectral properties. Evaluation was performed on the validation set, ensuring no overlap with the test set utilized in Sec. 4.1.

Wavelength Positional Encoding. The influence of wavelength positional encoding, a core component of the proposed spectral encoder, and its associated hyperparameter, σ , as defined in Eq. (1), was investigated. Larger values of σ introduce higher frequency components into the positional encoding [35], leading to an intrinsic relationship between this parameter and the spectral resolution of the input image. Tab. 3a shows that without wavelength positional

	mIoU	# Query Rep.	mIoU
No PE	18.3	$K = 1$	57.8
PE with $\sigma = 1$	55.1	$K = 4$	58.2
PE with $\sigma = 3$	61.5	$K = 8$	63.9
PE with $\sigma = 10$	57.2	$K = 16$	62.2

(a) Wavelength positional encoding (PE) enables cross-camera generalization.

(b) An increasing number of query representation leads to higher model capacity.

Table 3. Ablation on wavelength positional encoding and number of query representations.

encoding, the model fails to establish channel correspondences across cameras. Furthermore, $\sigma = 3$ yielded best performance, suggesting a balanced trade-off between high and low frequency components.

Number of Query Representations. The second critical component of the proposed spectral encoder is the compression of spectral data into learned query representations. While augmenting the number of query representations can potentially increase model capacity, it concurrently elevates computational complexity. The findings in Tab. 3b demonstrate a substantial performance improvement with a minimum of $K = 8$ queries.

6. Conclusion

In this work, we introduced CARL, the first camera-agnostic framework for spectral image analysis that unifies RGB, multispectral, and hyperspectral modalities within a single, robust representation learning paradigm. By leveraging wavelength-aware positional encoding and a novel query-based spectral encoder, CARL effectively bridges the gap between spectrally diverse imaging devices. We further proposed CARL-SSL, a tailored self-supervised learning strategy that jointly captures spectral and spatial semantics without reliance on manual annotations. Extensive experiments across medical imaging, autonomous driving, and

satellite remote sensing demonstrate CARL’s superior generalization under spectral heterogeneity and its scalability across domains and modalities. Our approach outperforms existing methods while significantly reducing reliance on homogeneous training data, laying a foundation for future spectral vision foundation models. By unlocking the untapped potential of cross-camera spectral datasets, CARL paves the way toward a more universal and accessible future in spectral imaging.

Acknowledgments

This project was supported by the European Research Council (ERC) under the European Union’s Horizon 2020 research and innovation programme (NEURAL SPICING, 101002198), the German Federal Ministry of Education and Research (6GHealth, 16KISK227), the National Center for Tumor Diseases (NCT), Heidelberg’s Surgical Oncology Program, the German Cancer Research Center (DKFZ), and the Helmholtz Association under the joint research school HIDSS4Health (Helmholtz Information and Data Science School for Health). We also acknowledge the support through state funds for the Innovation Campus Health + Life Science Alliance Heidelberg Mannheim from the structured postdoc program for Alexander Studier Fischer: Artificial Intelligence in Health (AIH).

References

- [1] Mahmoud Assran, Quentin Duval, Ishan Misra, Piotr Bojanowski, Pascal Vincent, Michael Rabbat, Yann LeCun, and Nicolas Ballas. Self-supervised learning from images with a joint-embedding predictive architecture. In *CVPR*, pages 15619–15629, 2023. [2](#), [3](#), [4](#), [5](#), [11](#)
- [2] Leonardo Ayala, Tim J Adler, Silvia Seidlitz, Sebastian Wirkert, Christina Engels, Alexander Seitel, Jan Sellner, Alexey Aksenov, Matthias Bodenbach, Pia Bader, et al. Spectral imaging enables contrast agent-free real-time ischemia monitoring in laparoscopic surgery. *Science advances*, 9(10):eadd6778, 2023. [1](#)
- [3] Adrien Bardes, Jean Ponce, and Yann LeCun. Vircreg: Variance-invariance-covariance regularization for self-supervised learning. *arXiv preprint arXiv:2105.04906*, 2021. [5](#), [11](#)
- [4] Koldo Basterretxea, Victoria Martínez, Javier Echanobe, Jon Gutiérrez-Zaballa, and Inés Del Campo. Hsi-drive: A dataset for the research of hyperspectral image processing applied to autonomous driving systems. In *2021 IEEE Intelligent Vehicles Symposium (IV)*, pages 866–873. IEEE, 2021. [7](#)
- [5] Alexander Baumann, Leonardo Ayala, Alexander Studier-Fischer, Jan Sellner, Berkin Özdemir, Karl-Friedrich Kowalewski, Slobodan Ilic, Silvia Seidlitz, and Lena Maier-Hein. Deep intra-operative illumination calibration of hyperspectral cameras. In *International Conference on Medical Image Computing and Computer-Assisted Intervention*, pages 120–131. Springer, 2024. [2](#)
- [6] Nassim Ait Ali Braham, Conrad M Albrecht, Julien Mairal, Jocelyn Chanussot, Yi Wang, and Xiao Xiang Zhu. Spectraearth: Training hyperspectral foundation models at scale. *arXiv preprint arXiv:2408.08447*, 2024. [2](#), [6](#), [11](#), [12](#)
- [7] Mathilde Caron, Hugo Touvron, Ishan Misra, Hervé Jégou, Julien Mairal, Piotr Bojanowski, and Armand Joulin. Emerging properties in self-supervised vision transformers. In *ICCV*, pages 9650–9660, 2021. [1](#), [3](#)
- [8] Zhe Chen, Yuchen Duan, Wenhai Wang, Junjun He, Tong Lu, Jifeng Dai, and Yu Qiao. Vision transformer adapter for dense predictions. In *The Eleventh International Conference on Learning Representations*, 2023. [5](#), [11](#)
- [9] Bowen Cheng, Ishan Misra, Alexander G Schwing, Alexander Kirillov, and Rohit Girdhar. Masked-attention mask transformer for universal image segmentation. In *CVPR*, pages 1290–1299, 2022. [7](#), [11](#)
- [10] Yezhen Cong, Samar Khanna, Chenlin Meng, Patrick Liu, Erik Rozi, Yutong He, Marshall Burke, David Lobell, and Stefano Ermon. Satmae: Pre-training transformers for temporal and multi-spectral satellite imagery. In *NeurIPS*, pages 197–211. Curran Associates, Inc., 2022. [2](#), [3](#), [8](#)
- [11] Marius Cordts, Mohamed Omran, Sebastian Ramos, Timo Rehfeld, Markus Enzweiler, Rodrigo Benenson, Uwe Franke, Stefan Roth, and Bernt Schiele. The cityscapes dataset for semantic urban scene understanding. In *Proceedings of the IEEE conference on computer vision and pattern recognition*, pages 3213–3223, 2016. [7](#), [11](#)
- [12] Jia Deng, Wei Dong, Richard Socher, Li-Jia Li, Kai Li, and Li Fei-Fei. Imagenet: A large-scale hierarchical image database. In *2009 IEEE conference on computer vision and pattern recognition*, pages 248–255. Ieee, 2009. [11](#)
- [13] Jacob Devlin, Ming-Wei Chang, Kenton Lee, and Kristina Toutanova. Bert: Pre-training of deep bidirectional transformers for language understanding. In *Proceedings of the 2019 conference of the North American chapter of the association for computational linguistics: human language technologies, volume 1 (long and short papers)*, pages 4171–4186, 2019. [1](#), [5](#)
- [14] Alexey Dosovitskiy, Lucas Beyer, Alexander Kolesnikov, Dirk Weissenborn, Xiaohua Zhai, Thomas Unterthiner, Mostafa Dehghani, Matthias Minderer, Georg Heigold, Sylvain Gelly, Jakob Uszkoreit, and Neil Houlsby. An image is worth 16x16 words: Transformers for image recognition at scale. In *ICLR*, 2021. [2](#), [3](#), [4](#), [5](#)
- [15] Yuxin Fang, Quan Sun, Xinggang Wang, Tiejun Huang, Xinlong Wang, and Yue Cao. Eva-02: A visual representation for neon genesis. *Image and Vision Computing*, 149:105171, 2024. [5](#), [11](#), [12](#)
- [16] Martin Hermann Paul Fuchs and Begüm Demir. Hyspecnet-11k: A large-scale hyperspectral dataset for benchmarking learning-based hyperspectral image compression methods. In *IGARSS 2023-2023 IEEE International Geoscience and Remote Sensing Symposium*, pages 1779–1782. IEEE, 2023. [7](#)
- [17] Yuval Garini, Ian T Young, and George McNamara. Spectral imaging: principles and applications. *Cytometry part a: the journal of the international society for analytical cytology*, 69(8):735–747, 2006. [13](#)

- [18] Jie Gui, Tuo Chen, Jing Zhang, Qiong Cao, Zhenan Sun, Hao Luo, and Dacheng Tao. A survey on self-supervised learning: Algorithms, applications, and future trends. *IEEE TPAMI*, 2024. 3
- [19] Renlong Hang, Qingshan Liu, Danfeng Hong, and Pedram Ghamisi. Cascaded recurrent neural networks for hyperspectral image classification. *IEEE Transactions on Geoscience and Remote Sensing*, 57(8):5384–5394, 2019. 2
- [20] Kaiming He, Xiangyu Zhang, Shaoqing Ren, and Jian Sun. Deep residual learning for image recognition. In *CVPR*, pages 770–778, 2016. 1
- [21] Kaiming He, Haoqi Fan, Yuxin Wu, Saining Xie, and Ross Girshick. Momentum contrast for unsupervised visual representation learning. In *CVPR*, pages 9729–9738, 2020. 1, 3
- [22] Kaiming He, Xinlei Chen, Saining Xie, Yanghao Li, Piotr Dollár, and Ross Girshick. Masked autoencoders are scalable vision learners. In *CVPR*, pages 16000–16009, 2022. 1, 3, 11
- [23] Danfeng Hong, Zhu Han, Jing Yao, Lianru Gao, Bing Zhang, Antonio Plaza, and Jocelyn Chanussot. Spectralformer: Rethinking hyperspectral image classification with transformers. *IEEE Transactions on Geoscience and Remote Sensing*, 60:1–15, 2021. 2
- [24] Danfeng Hong, Bing Zhang, Xuyang Li, Yuxuan Li, Chenyu Li, Jing Yao, Naoto Yokoya, Hao Li, Pedram Ghamisi, Xiuping Jia, et al. Spectralgpt: Spectral remote sensing foundation model. *IEEE TPAMI*, 2024. 2, 3, 7, 8, 11, 12
- [25] Jared Kaplan, Sam McCandlish, Tom Henighan, Tom B Brown, Benjamin Chess, Rewon Child, Scott Gray, Alec Radford, Jeffrey Wu, and Dario Amodei. Scaling laws for neural language models. *arXiv preprint arXiv:2001.08361*, 2020. 2
- [26] Yann LeCun. A path towards autonomous machine intelligence version 0.9. 2, 2022-06-27. *Open Review*, 62(1):1–62, 2022. 5
- [27] Junnan Li, Dongxu Li, Silvio Savarese, and Steven Hoi. Blip-2: Bootstrapping language-image pre-training with frozen image encoders and large language models. In *International conference on machine learning*, pages 19730–19742. PMLR, 2023. 4
- [28] Ze Liu, Yutong Lin, Yue Cao, Han Hu, Yixuan Wei, Zheng Zhang, Stephen Lin, and Baining Guo. Swin transformer: Hierarchical vision transformer using shifted windows. In *ICCV*, pages 10012–10022, 2021. 4, 7
- [29] Bing Lu, Phuong D Dao, Jiangui Liu, Yuhong He, and Jiali Shang. Recent advances of hyperspectral imaging technology and applications in agriculture. *Remote Sensing*, 12(16):2659, 2020. 1
- [30] Maxime Oquab, Timothée Darcet, Théo Moutakanni, Huy Vo, Marc Szafraniec, Vasil Khalidov, Pierre Fernandez, Daniel Haziza, Francisco Massa, Alaaeldin El-Nouby, et al. Dinov2: Learning robust visual features without supervision. *arXiv preprint arXiv:2304.07193*, 2023. 11
- [31] Shen-En Qian. Hyperspectral satellites, evolution, and development history. *IEEE Journal of Selected Topics in Applied Earth Observations and Remote Sensing*, 14:7032–7056, 2021. 1
- [32] Linus Scheibenreif, Michael Mommert, and Damian Borth. Masked vision transformers for hyperspectral image classification. In *Proceedings of the IEEE/CVF conference on computer vision and pattern recognition*, pages 2166–2176, 2023. 3
- [33] Silvia Seidlitz, Jan Sellner, Jan Odenthal, Berkin Özdemir, Alexander Studier-Fischer, Samuel Knödler, Leonardo Ayala, Tim J Adler, Hannes G Kenngott, Minu Tizabi, et al. Robust deep learning-based semantic organ segmentation in hyperspectral images. *Medical Image Analysis*, 80:102488, 2022. 1, 2, 6
- [34] Qiu Shen, Yuxing Huang, Tianqi Ren, Ying Fu, and Shaodi You. Urban scene understanding via hyperspectral images: Dataset and benchmark. *Available at SSRN 4560035*. 1, 7
- [35] Matthew Tancik, Pratul Srinivasan, Ben Mildenhall, Sara Fridovich-Keil, Nithin Raghavan, Utkarsh Singhal, Ravi Ramamoorthi, Jonathan Barron, and Ren Ng. Fourier features let networks learn high frequency functions in low dimensional domains. *NeurIPS*, 33:7537–7547, 2020. 4, 8
- [36] Nick Theisen, Robin Bartsch, Dietrich Paulus, and Peer Neubert. Hs3-bench: A benchmark and strong baseline for hyperspectral semantic segmentation in driving scenarios. In *2024 IEEE/RSJ International Conference on Intelligent Robots and Systems (IROS)*, pages 5895–5901. IEEE, 2024. 1, 2
- [37] Prasad S Thenkabail, John G Lyon, and Alfredo Huete. Advances in hyperspectral remote sensing of vegetation and agricultural crops. In *Fundamentals, sensor systems, spectral libraries, and data mining for vegetation*, pages 3–37. CRC press, 2018. 1
- [38] Leon Amadeus Varga, Martin Messmer, Nuri Benbarka, and Andreas Zell. Wavelength-aware 2d convolutions for hyperspectral imaging. In *Proceedings of the IEEE/CVF Winter Conference on Applications of Computer Vision*, pages 3788–3797, 2023. 2, 6, 11, 12
- [39] Ashish Vaswani, Noam Shazeer, Niki Parmar, Jakob Uszkoreit, Llion Jones, Aidan N Gomez, Łukasz Kaiser, and Illia Polosukhin. Attention is all you need. In *NeurIPS*. Curran Associates, Inc., 2017. 4
- [40] Christian Winkens, Florian Sattler, Veronika Adams, and Dietrich Paulus. Hyko: A spectral dataset for scene understanding. In *Proceedings of the IEEE International Conference on Computer Vision Workshops*, pages 254–261, 2017. 7
- [41] Tete Xiao, Yingcheng Liu, Bolei Zhou, Yuning Jiang, and Jian Sun. Unified perceptual parsing for scene understanding. In *Proceedings of the European conference on computer vision (ECCV)*, pages 418–434, 2018. 5, 11

Appendix

A. Implementation Details

We begin by outlining general implementation details of CARL. In our experiments, we utilized a small version of CARL, comprising overall 12 attention blocks with an embedding dimension of 384. The blocks were structured into $L = 4$ self-attention-cross-attention modules within the spectral encoder and 8 self-attention blocks within the spatial encoder. To incorporate wavelength information in the positional encoding, the wavelengths were given in nanometers, and scaled by a factor of $\alpha = 10^{-3}$, to obtain position coordinates approximately in the range of one. In accordance with the ablation studies presented in the main manuscript, the hyperparameter σ in the wavelength positional encoding was set to 3 and $K = 8$ query representations were employed. The initial convolution in our model utilized a kernel size and stride of 8, resulting in patch dimensions of 8×8 . The query representations within the spectral encoder were implemented as learnable embeddings, initialized using a truncated normal distribution with a mean of zero and a standard deviation of 0.5. Furthermore, a 1D sinusoidal positional encoding scheme, based on discrete token positions, was implemented to represent the positions of $(Q_j)_{j \leq K}$.

A.1. Implementation Details of Downstream Tasks

In the first and third experiment, CARL was integrated with the ViTAdapter [8] to generate hierarchical features, which were subsequently forwarded to the UperNet segmentation head [41]. The ViTAdapter applies lightweight convolutions to the input and facilitates information exchange with the spatial transformer via injector and extractor modules. To maintain invariance with respect to the channel dimensionality, a single channel of the given spectral image was used as input to these convolutions. The rationale behind this approach is to leverage the enhanced spatial resolution provided by the convolutions, as the encoded spectral information is contained within the camera-agnostic representation of CARL. As segmentation loss, an equally weighted sum of the cross entropy loss and the dice loss was employed. To enhance training stability, the attention blocks within the spectral encoder were initialized using Dinov2 weights [30], which provide a robust checkpoint derived from self-supervised large-scale training. The spatial encoder, EVA-02 [15], was initialized with self-supervised weights obtained through masked image modeling [22] on ImageNet [12]. Furthermore, the model was optimized using the AdamW optimizer with an initial learning rate of 10^{-4} . An exponential learning rate scheduler was employed to reduce the learning rate throughout the training process.

Model	# Parameters	# FLOPs
EVA-02 [15]	22.8M	6.4G
Hyve [38]	21.8M	6.4G
Spectral Adapter [6]	23.0M	22.7G
SpectralGPT ⁺ [24]	21.5M	242.1G
CARL	28.9M	120.5G

Table 4. **Our model effectively balances model capacity and computational complexity.** The number of floating-point operations (FLOPs) are compared among camera-specific and channel-invariant models for spectral imaging. Models with a dedicated spectral encoding strategy exhibit substantially higher computational costs. However, CARL maintains a lower FLOP count than SpectralGPT⁺.

The training procedure of the second experiment followed that of the original Mask2Former [9] training on Cityscapes [11].

In all experiments, a channel sampling strategy was employed to reduce the GPU memory consumption during training. Specifically, in instances where the channel dimension of the spectral image surpassed 32, a random sub-sampling of 32 channels was performed. Crucially, this did not affect performance, as the spectral tokens are ordered via wavelength positional encoding. As a result, all experiments were successfully executed on a single GPU endowed with a memory capacity of up to 32 gigabytes.

A.2. Implementation Details of SSL-Pre-Training

The model subject to pre-training consisted of the proposed spectral encoder, in conjunction with the EVA-02 spatial encoder. As outlined in the main manuscript, the pre-training strategy employs spectral and spatial masking with reconstruction objectives in the feature space through predictors. To manage training resources, 16 channels per image were sampled during training. Spectral self-supervision utilized two masks, each covering from 15 % to 20 % of the channel dimensionality. Utilizing the I-JEPA configurations [1], the spatial self-supervision employed four masks, each ranging from 15 % to 20 % of the spatial dimensions. The predictors are transformer architectures with a depth of 3 and an embedding dimension of 384. The loss function is composed of equally weighted spectral and spatial components. Both, spectral and spatial self-supervision leverage the VICReg loss [3], which is decomposed into invariance, variance, and covariance terms. Following the recommendations of the original work, weights of 1 were assigned to the invariance and variance terms, and a weight of 0.05 was assigned to the covariance term. Optimization was performed using the AdamW optimizer with an initial learning rate of 10^{-4} , and a cosine annealing learning rate scheduler with exponentially decaying amplitude.

	Camera-specific	Spectral Adapter [6]	Hyve [38]	CARL	CARL-SSL
Road	93.4	93.6	94.0	94.7	95.0
Sidewalk	32.8	33.5	44.3	43.5	47.8
Building	69.8	54.9	69.4	71.1	71.1
Wall	55.1	43.9	54.4	55.4	55.2
Fence	14.1	5.3	11.5	11.3	13.9
Pole	0.0	29.6	20.8	31.0	31.8
Traffic light	51.0	50.4	53.0	55.5	57.2
Traffic sign	53.4	49.4	54.6	59.1	61.5
Vegetation	80.9	72.5	80.9	82.0	81.9
Terrain	3.2	9.0	3.6	6.6	5.1
Sky	85.8	79.9	87.2	88.4	88.7
Person	30.9	28.0	36.0	29.6	31.9
Rider	34.0	34.3	44.5	32.2	37.8
Car	86.0	88.1	88.0	89.3	90.3
Truck	53.7	50.8	60.6	57.5	63.0
Bus	67.6	80.0	80.3	87.6	87.4
Train	-	-	-	-	-
Motorcycle	0.0	0.4	0.0	0.0	0.0
Bicycle	36.0	20.0	29.1	29.1	33.1
mIoU	44.6 [40.9; 47.3]	43.4 [41.0; 45.2]	48.0 [45.4; 50.0]	48.6 [45.6; 51.0]	50.1 [47.2; 52.4]

Table 5. **The proposed spectral encoder demonstrates superior performance as a camera-agnostic model.** The class-wise IoU scores with the 95 % confidence intervals of the mIoU scores on the HSICity test set. While the camera-specific model was pre-trained on Cityscapes and fine-tuned exclusively on HSICity, the other models are channel-invariant adaptations which were concurrently trained on both datasets. Notably, our spectral encoder performs best among the presented adaptation methods, and significantly benefits from self-supervised pre-training.

B. Computational Complexity

Encoding high-dimensional spatial-spectral data requires substantial computational resources; thus, preventing floating-point operation (FLOP) overflow is crucial. We conducted a comparative analysis of FLOPs across spectral imaging models, ensuring fairness by standardizing embedding dimension and depth of the models, and evaluating only the backbone encoder. Notably, CARL, the Hyve layer [38], and the Spectral Adapter [6] were integrated with the spatial backbone EVA-02 [15]. Additionally, we included SpectralGPT⁺ [24] to the analysis. We evaluated the FLOPs for a spectral image of size $128 \times 128 \times 48$, acknowledging that the benchmarked models exhibit varying scalability with spatial and spectral dimensions. The results in Tab. 4 demonstrate that the basic EVA-02 model and its Hyve layer adaptation demonstrate the lowest FLOPs. This is attributable to their limitation to spatial encoding. Conversely, the Spectral Adapter, SpectralGPT⁺, and our proposed model are specifically designed for comprehensive spectral encoding. While the Spectral Adapter utilizes 1D convolutions along the spectral dimension, resulting in a relatively low FLOP count, SpectralGPT⁺ employs 3D patching and self-attention across spatio-spectral patches. Consequently, SpectralGPT⁺ exhibits the highest computational cost, as evidenced in Tab. 4. Notably, its FLOP count is approximately double that of CARL, which also

extensively encodes the spectral dimension but utilizes a more computationally efficient approach. In particular, our model performs cross-attention between the query representations and the channels, scaling only linearly with the spectral dimension. Thus, our model not only achieved superior performance compared to SpectralGPT⁺ but also demonstrated a significant reduction in FLOPs, establishing a favorable trade-off between model capacity and computational complexity.

C. Urban Scene Segmentation

The detailed class-wise IoU scores on the HSICity test set are depicted in Tab. 5. CARL and CARL-SSL exhibited superior performance benchmarked against camera-specific and channel-invariant spectral imaging models. As the HSICity training set does not contain any "pole" annotation, the camera-specific model exhibits a "pole" IoU score of 0. Notably, CARL-SSL achieved the best IoU score for the "pole" class with 31.8 mIoU, indicating superior capability of translating RGB labels from Cityscapes to hyperspectral imagery.

D. Multispectral Synthetic Data Generation

As outlined in Sec. 4.1 of the main manuscript, we synthesized multispectral images from given hyperspectral images to simulate spectral heterogeneity within the training

set. This section provides a more in-depth explanation of the data generation procedure.

In spectral imaging, optical filters play a crucial role in isolating specific wavelength bands to capture reflectance values, as also described in [17]. The filters selectively transmit light within predefined wavelength ranges, which are determined by their material properties and design specifications. The transmission characteristics of an optical filter are typically described by its filter function, which quantifies the transmitted intensity as a function of wavelength. In our approach, we generated virtual multispectral cameras through the modeling of filter functions using Gaussian distributions, thereby enabling the synthesis of corresponding multispectral images from provided hyperspectral images.

Specifically, we simulated a multispectral channel by first sampling the corresponding filter's center wavelength μ through farthest point sampling within [550 nm, 950 nm], and the variance σ uniformly within [5, 25]. As the given hyperspectral images exhibited wavelengths from 500 nm to 1,000 nm with 5 nm steps, we discretized the wavelength axis accordingly and set $\lambda = (500, 505, \dots, 995)^T \in \mathbb{R}^{100}$. Then, we defined the L1-normalized filter function $\tilde{F}_{\mu,\sigma}$ as following:

$$F_{\mu,\sigma}(\lambda_i) = e^{-\frac{(\lambda_i - \mu)^2}{2\sigma^2}} \quad (2)$$

$$\tilde{F}_{\mu,\sigma}(\lambda_i) = \frac{F_{\mu,\sigma}(\lambda_i)}{\sum_{j=1}^{100} |F_{\mu,\sigma}(\lambda_j)|} \quad (3)$$

By uniformly sampling the number of channels, C , within [10, 25], we obtained C channel-specific filter functions, as described above. These functions can be collectively represented in matrix form as follows:

$$\tilde{F} = \begin{bmatrix} \tilde{F}_{1,\mu,\sigma}(\lambda)^T \\ \vdots \\ \tilde{F}_{C,\mu,\sigma}(\lambda)^T \end{bmatrix} \in \mathbb{R}^{C \times 100} \quad (4)$$

Finally, for a hyperspectral pixel $P_{HSI} \in \mathbb{R}^{100}$, we simulated the corresponding multispectral pixel by:

$$P_{MSI} = \tilde{F} \cdot P_{HSI} \in \mathbb{R}^C \quad (5)$$

This matrix-vector multiplication can be performed for each pixel, leading to an multispectral image with C channels. Notably, we only altered spectral properties of the images, while preserving geometric information.